Journal of Catalysis **204,** 118–128 (2001)
doi:10.1006/jcat.2001.3366, available online at http://www.idealibrary.com on IDEAL®

NO Reduction by CO on the Pt(100) Surface

A Density Functional Theory Study

A. Eichler and J. Hafner

Institut für Materialphysik and Center for Computational Materials Science, Universität Wien, Sensengasse 8/12, A-1090 Wien, Austria
E-mail: andreas.eichler@univie.ac.at

Received March 26, 2001; revised July 25, 2001; accepted July 25, 2001

NO reduction belongs to the most important reactions in environmental and industrial catalysis. In this study the NO reduction accompanied by the simultaneous oxidation of CO over a platinum catalyst is investigated on the basis of ab-initio calculations. The whole reaction cycle is broken up into several reaction steps (CO and NO adsorption, NO dissociation, N_2 desorption, CO oxidation, CO_2 desorption). Each of these subprocesses is characterized by calculating transition state, adsorption/activation energy, prefactor, and rate constant, so that finally a consistent picture of the overall reaction on an atomistic scale is obtained. NO dissociation is found to be rate limiting with an activation barrier of $E^0_{act} = 1.21$ eV and a prefactor of $\nu = 2.1 \cdot 10^{12}$ ML $\cdot$ s^{-1}; N_2 desorption is an essentially barrierless process, while the CO oxidation step itself can be described by an activation energy of $E^0_{act} = 0.83$ eV and a prefactor of $\nu = 2.0 \cdot 10^{12}$ ML $\cdot$ s^{-1}.

Key Words: **density functional calculations; models of surface chemical reactions; catalysis; oxidation; platinum; carbon monoxide; nitrogen oxides.**

1. INTRODUCTION

The reduction of NO_x belongs to the most important tasks of environmental chemistry. In the easiest case NO reacts with carbon monoxide forming half a N_2 molecule and carbon dioxide,

$$CO + NO \rightarrow \frac{1}{2}N_2 + CO_2. \qquad [1]$$

Besides many other applications, this reaction is one of the key processes in car exhaust catalysts, where it is promoted by a Pt–Rh surface (1). Although there is great industrial interest, knowledge on an atomic scale is very limited. Even less is known of the role of the catalyst itself. In this study the reaction on a Pt(100) surface is modeled using ab-initio total-energy calculations. We have investigated the potential energy surface on which the reaction takes place, identified transition states (TS) and barriers for the subprocesses, and calculated reaction rate constants on the basis of harmonic transition-state theory. This particular low-index platinum surface has been chosen for several reasons: the reactivity of the three low-index surfaces is very different: while no reaction occurs on the Pt(111) surface (2), reaction rates are already significant on the more open (110) face. On the investigated (100) surface the reaction takes place in an explosive manner when heating a co-adsorption phase of CO and NO (3). These differences in promoting the NO/CO reaction are directly related to the ability of the surface to dissociate NO (4). A further interesting feature of the reaction on this particular surface is the oscillatory behavior in time of the CO_2 desorption signal under certain experimental conditions (5–7).

Our paper is organized as follows: after the sections on the experimental status and the methodology of our calculations, we start with the characterization of the adsorption of reactants and intermediates (NO, CO, N, O) on the surface. The following section deals with the calculation of the reaction barriers for the subprocesses: dissociation of NO (the key process of the reaction), the desorption of N_2, and finally, CO oxidation. In addition, we also briefly consider a direct reaction between NO and CO. In the following section all pieces of information are put together, so that the complete energetics of the reaction can be described. Section 7 is devoted to a kinetic description of the reaction on the basis of harmonic transition-state theory. The paper closes with a summary of the results.

2. PREVIOUS EXPERIMENTAL STUDIES

A clean Pt(100) surface undergoes a quasi-hexagonal reconstruction (8, 9), which is lifted immediately upon adsorption of small amounts of NO (10) or CO (11, 12). Both gases show a tendency toward island formation on the surface, adsorbed separately (10–13) as well for the co-adsorption phase (14). The formation of this NO/CO overlayer does not depend on which of the gases is adsorbed first and leads to a downshift in the stretch frequencies of both adsorbates (14). Heating up the overlayer leads to the already mentioned surface explosion, i.e., the desorption

0021-9517/01 $35.00

of CO_2 and N_2 at around 410 K (15). The second peculiarity is the oscillatory manner in which this reaction takes place. Within two separate pressure/temperature regimes CO_2 signals with a period of about 30 s have been detected (7). In the higher temperature regime the reaction is always accompanied by a surface reconstruction into the hex phase (as is the case for the surface explosion). From that it has been concluded that this surface (de-)reconstruction mechanism is the reason for the oscillating reaction behavior, since higher adsorption energies have been determined for the dereconstructed (1×1) surface, favoring island formation on dereconstructed facets of the surface. However, the reaction takes place on a perfect (1×1)-surface for the lower temperature regime of the oscillatory behavior (16). Furthermore the same reaction was observed on Pd (100), without a combined surface reconstruction (17). These two observations provide strong evidence that the surface reconstruction is not required for the present reaction. The reconstruction mechanism may only support the formation of the islands due to higher adsorption energies of both gases on the (1×1) phase of the surface (12, 18).

Besides models involving the discussed surface (de)reconstruction and intermediate species (15) to explain the autocatalytic behavior, the most realistic model is the so-called vacancy requirement for the NO-dissociation (19) (asterisks denote an empty surface site, asterisks in superscripts refer to adsorbed species):

$$\begin{aligned} CO + * &\leftrightarrow CO^* \\ NO + * &\leftrightarrow NO^* \\ NO^* + * &\rightarrow N^* + O^* \\ N^* + N^* &\rightarrow N_2 + 2* \\ CO^* + O^* &\rightarrow CO_2 + 2*. \end{aligned} \qquad [2]$$

The first two steps of the reaction are the adsorption of CO and NO at the surface. Each of the processes consumes an empty surface site. Islands of adsorbates are formed and grow until all sites are occupied and no more vacant surface sites are left. Hence the next step, the dissociation of NO, which requires an additional surface site, is inhibited until one of the adsorbed gases starts to desorb. Then dissociation can take place, followed immediately by N_2 desorption and CO oxidation. Both reaction steps provide two additional vacant sites, so that the $CO^* + NO^*$ subprocess can continue until all CO and NO has reacted forming N_2 and CO_2. In the sense that it produces more vacant surface sites $(4*)$ than it requires $(1*)$ this subprocess is autocatalytic.

Based on this model and experimental estimates for the desorption and activation energies the reaction has been modeled by coupled differential equations (18, 19) and on the basis of lattice-gas Hamiltonians (20). The fine tuning of the experimental estimates used in these simulations to reproduce the observed reaction behavior provides a complete set of activation energies and prefactors of high reliability.

3. METHODOLOGY

The calculations are performed using the Vienna ab-initio simulation package VASP (21) which is a density-functional-theory (DFT) code, working in a plane wave basis set. Electron–ion interaction is described using ultra soft pseudo-potentials (22) for N, C, O, and Pt with a cut-off energy of $E_{\text{cut}} = 350$ eV. For exchange and correlation the functional proposed by Perdew and Zunger (23) is used, adding (nonlocal) generalized gradient corrections (GGA). First, we did the complete investigation of the reaction (including adsorption/activation energies, prefactors, rate constants) employing the PW91-GGA (24). However, because of the reported improvement in adsorption energies within the recently proposed RPBE functional (25), we recalculated all relevant energies with this new functional at fixed PW91-GGA geometries. For that reason in the first part of the study, where extensive investigation for different adsorption structures are reported, mainly results for the PW91-GGA are given. However, in the second part describing the reaction itself, all relevant results are given for both functionals so that a consistent description of the reaction can be given within both functionals and a comparison is possible. In test calculations for CO and NO adsorption, we found energy differences of less than 5 meV when using geometries, lattice constants, and pseudo-potentials from the PW91-GGA and only recalculating the energies (self-consistently) using the RPBE-GGA compared to a consistent treatment (pseudo-potential, lattice constant, structural optimization) within the new functional. Furthermore optimized adsorption structures in PW91 and RPBE differ by less than 1%. The change in energy when switching between two rather different GGA functionals can also serve as an estimate for the error bars induced by the approximations in the exchange correlation functional.

The substrate is modeled by two different cells: for higher coverage we use a $c(2 \times 4)$ cell with four substrate layers, for configurations at lower coverage a $p(3 \times 2)$ cell, with a reduced thickness of only three layers for which the consistency with the four layer slab was checked. Both cells are depicted in Fig. 1 together with a $c(2 \times 2)$ cell used

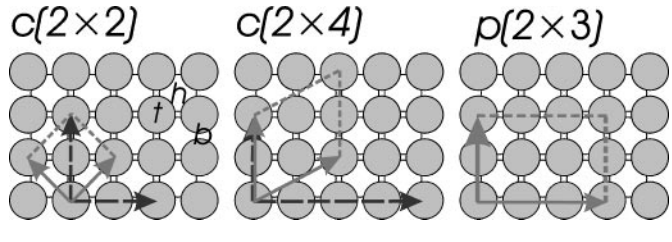

FIG. 1. Sketch of the surface cells used within these calculations.

for CO adsorption. Subsequent cells are separated in the z-direction by a 14-Å wide vacuum layer. Surface relaxation effects have been neglected in most of the calculations. Although Henkelman and Jónsson have shown very recently the importance of substrate relaxation and system size (in terms of layers) for the dissociative adsorption of methane over Ir(111) (26) we could not observe such a behaviour for the actual system. Also our experience from previous calculations for the adsorption of O_2 on Pt(111) (27), CO on Pt(111), and CO on Rh(100) (28) and Pd(100) (29) shows that there exists only a minor influence of the substrate relaxation on the energetics (<100 meV) and geometry of the adsorbate (<0.1 Å). However, in the case of the reaction barriers the influence is investigated explicitly. Brillouin-zone integrations are performed on a grid of $(4 \times 3 \times 1)$ $[(3 \times 2 \times 1), (6 \times 6 \times 1)]$ $\vec{k}$-points for the $c(2 \times 4)$ $[p(2 \times 3), c(2 \times 2)]$ cell using a Methfessel–Paxton smearing of second-order (30) with a width of $\sigma = 0.2$ eV. All calculations are done at the equilibrium lattice constant $a^{\mathrm{PW91}} = 3.99$ Å (exp.: $a^{\mathrm{exp}} = 3.92$ Å). The energy balance for the complete gas-phase reaction (Eq. [1]) based on the binding energies of the molecules is $\Delta E^{\mathrm{calc}}_{\mathrm{PW91}} = 4.41$ eV ($\Delta E^{\mathrm{calc}}_{\mathrm{RPBE}} = 3.50$ eV) compared to the experimental value of $\Delta E^{\mathrm{exp}} = 3.82$ eV. The deviation compared to the experiment can be predominantly explained by the difficulty of the DFT in describing free molecules, because of high density gradients. These errors are reduced in the GGA, but still present. However, the description for adsorbed species and hence also for reaction and dissociation barriers is much better, as we will demonstrate within this study.

Frequencies have been calculated by diagonalization of the dynamical matrix from finite displacements. All stretch frequencies given in the adsorption section correspond therefore to in-phase vibrations, due to the periodic boundary conditions.

To calculate the dissociation barriers, transition states have been determined using the nudged elastic band method (NEB) (31, 32). In this method the total energies of a series of intermediate states distributed along the reaction path connecting the starting and final states are simultaneously minimized restricting the atomic motions to the hyperplane perpendicular to the reaction path. We used this method already successfully to determine reaction barriers in the CO oxidation reaction on Pt(111) (33).

For the activation energies we recalculated only initial, final, and transition states within the RPBE functional. For this reason the reaction pathways in Figs. 4–8 are only given for the PW91 functional. However, the corresponding RPBE curves are—besides an upshift in energy—similar.

4. ADSORPTION OF SINGLE SPECIES

The first step of the reaction is the adsorption of the reactants. Since nearly all adsorbates lift the hexagonal surface reconstruction immediately already in small doses (10–12) any kind of surface reconstruction is neglected.

4.1. CO Adsorption

Experimentally CO was found to form $c(2 \times 2)$ islands with a local coverage of 0.5 ML already at low surface coverage (11, 12). Using electron energy loss spectroscopy (EELS) two species were determined at 1950 and 2000–2030 cm^{-1}, which were assigned to bridge and top adsorbed CO, respectively. The ratio of the bridge/on-top EELS intensities varies between 0.5 and 0.2 for coverages between 0 and 0.75 ML, with a minimum at half coverage combined with a $c(2 \times 2)$ LEED pattern (12). From this it was deduced that the $c(2 \times 2)$ islands are formed mainly by on-top adsorbed species. The (isosteric) adsorption energy estimated from temperature programmed desorption (TPD) is 1.65 and 1.45 eV for low and half coverage, respectively (12). Employing single crystal adsorption calorimetry (SCAC) measurements integral adsorption energies of 2.18 and 1.98 eV were obtained for coverages of 0.1 and 0.5 ML (34).

Our results for CO adsorption in various superstructures (see Fig. 1) are compiled in Table 1. According to the calculations the most stable site (at $\Theta = \frac{1}{2}$ ML) is the bridge position ($E^{\mathrm{PW91}}_{\mathrm{ads}} = 2.01$ eV), whereas the on-top site is 290 meV higher in energy. A similar DFT failure for site preference in CO adsorption has recently been discussed for the Pt(111) surface (35).

However, since we are interested mainly in the formation of the co-adsorption phase with NO (and the successive reaction), where CO occupies exclusively on-top sites, we will not go into detail concerning the site preference for exclusively CO adsorption. The stretch frequencies are in reasonable agreement with the measurements. Decreasing the coverage to $\Theta = \frac{1}{4}$ ML ($c(2 \times 4)$) and $\Theta = \frac{1}{6}$ ML ($p(2 \times 3)$) increases the adsorption energy to 1.76 and 1.82 eV, respectively for the on-top adsorbed species, while the adsorption geometry remains essentially unchanged.

Switching to the RPBE-GGA decreases the adsorption energy for the $c(2 \times 2)$ islands to 1.45 eV. However,

TABLE 1

Bond Lengths (d), Height of the Carbon Atom above the Surface (h), Stretch Frequency (ω), and Adsorption Energies for PW91-GGA ($E^{\mathrm{PW91}}_{\mathrm{ads}}$) for CO adsorbed On-Top (t), Bridged (b), and in Hollow Positions (h) on the Pt(100) Surface

Θ		1/2			1/4	1/6
site	(ML)	t	b	h	t	t
d	(Å)	1.16	1.18	1.19	1.16	1.16
h	(Å)	1.86	1.46	1.19	1.86	1.86
ω	(cm^{-1})	2000	1930	1860	—	—
$E^{\mathrm{PW91}}_{\mathrm{ads}}$	(eV)	1.72	2.01	1.41	1.76	1.82

the preference for bridge sites remains unaffected ($\Delta E_{\text{top-bridge}} = 185$ meV).

Due to the large variation in the experimentally determined adsorption energies a comparison is difficult. The RPBE-GGA values are much closer to the TPD values, whereas the higher PW91-GGA adsorption energies are in better agreement with the microcalorimetric results. However, there are two arguments in favor for the comparison with the SCAC data: first the TPD values give the differential (isosteric) adsorption energy at a fixed coverage, whereas in the SCAC data an integral adsorption energy is derived, taking into account the whole energy gain from zero coverage up to the half monolayer structure, which resembles the situation in the calculation. Second, SCAC is considered to be the more accurate method. So under the assumption, that the SCAC values are more accurate, the PW91-GGA leads to better adsorption energies.

4.2. NO Adsorption

Similar to CO also for NO adsorption island formation at a local coverage of $\frac{1}{2}$ ML was observed, resulting in a $c(2\times4)$ LEED pattern (10, 13). On the (1×1) surface only a single frequency peak at 1640 cm^{-1} was detected at this coverage ($\frac{1}{2}$ ML), which has been assigned to NO adsorbed between bridge and on-top sites, so that rows of NO molecules are formed.

We started our studies for the NO molecule by testing several surface sites at full coverage, results of which are compiled in Table 2. The bridge site is by far the most favored one ($E_{\text{ads}}^{\text{PW91}} = 1.69$ eV), followed by nearly degenerated on-top ($E_{\text{ads}}^{\text{PW91}} = 1.10$ eV) and hollow ($E_{\text{ads}}^{\text{PW91}} = 1.09$ eV) adsorption. In these calculations we took spin polarization into account. Magnetic moments on the NO molecule are lower than 0.4 μ_B and of nearly no influence to the energetics or the structural properties. These results justify the neglect of magnetism for further calculations. This strong preference for bridge adsorption explains our results for half coverage in the experimentally observed $c(2 \times 4)$ structure: Starting from the structure proposed in (10) (Fig. 2A) we performed a structural optimization of the adsorbates, leading to a configuration of exclusively

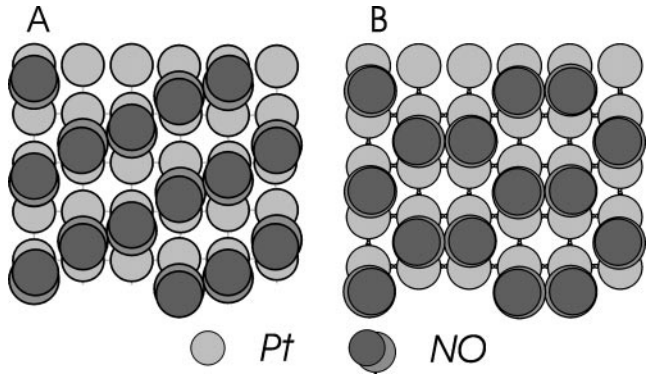

FIG. 2. Sketch of two possible NO configurations within a $c(2 \times 4)$ cell at $\Theta = 0.5$ ML.

bridge-adsorbed NO molecules in a pseudo-hexagonal arrangement (see Fig. 2B), with an adsorption energy of $E_{\text{ads}} = 2.07$ eV. Therefore we believe the experimentally observed $c(2 \times 4)$ LEED pattern has its origin in the structure sketched in Fig. 2B. Recalculating the adsorption energies within the RPBE-GGA leads to 1.65 eV. Reducing the coverage to $\Theta = \frac{1}{4}$ ML leaves the structural parameters nearly unchanged compared to the full-coverage structure, but the adsorption energy increases to $E_{\text{ads}} = 2.11$ eV. A further decrease of the coverage down to $\Theta = \frac{1}{6}$ ML at a $p(2 \times 3)$ structure increases the adsorption energy by another 60 meV to $E_{\text{ads}}^{\text{PW91}} = 2.17$ eV ($E_{\text{ads}}^{\text{RPBE}} = 1.84$ eV).

In comparison with experimental data, we encounter a dilemma similar to that in the CO adsorption case: whereas on the basis of TPD measurements a desorption energy of 1.48 eV at $\Theta = 0.5$ ML has been determined (4), a SCAC study reports 1.87 eV (34) for the integral adsorption energy. The differential value from SCAC (at $\Theta = 0.5$ ML) is substantially lower ($\sim$1.35 eV) and hence even below the isosteric TPD value. So also in the NO case it is difficult to determine which of the GGA functionals leads to a more realistic description of the adsorption properties.

In the same cell, we calculated the vibrational spectrum of the NO molecule at the surface (Table 3). The stretch frequency around 1585 cm^{-1} is in good agreement with a value of 1596 cm^{-1} for low coverage from (10). The lowest frequency is the frustrated translation toward the hollow site, much lower than, for example, the frustrated rotation in this direction. This indicates that this mode will initiate the dissociation process. It is also important to note that the change in the GGA functional induces only very small

TABLE 2

Bond Lengths (d), Height of the Nitrogen Atom above the Surface (h) and Adsorption Energies for PW91-GGA ($E_{\text{ads}}^{\text{PW91}}$) for NO Adsorbed On-Top (t), Bridged (b), and in Hollow Positions (h) on the Pt(100) Surface in a $p(1 \times 1)$ Arrangement ($\Theta = 1.0$ ML)

Θ		1			1/2	1/4	1/6
site	(ML)	t	b	h	b	b	b
d	(Å)	1.19	1.21	1.21	1.20	1.20	1.20
h	(Å)	1.85	1.38	1.33	1.39	1.37	1.37
$E_{\text{ads}}^{\text{PW91}}$	(eV)	1.10	1.69	1.09	2.07	2.11	2.17

TABLE 3

Frequency Spectrum (cm^{-1}) of NO Adsorbed in a $p(2 \times 3)$ Arrangement at $\Theta = \frac{1}{6}$ ML on a Pt(100) Surface

	$\omega_{\text{N-O}}$	ω_{r1}	$\omega_{\text{M-NO}}$	ω_{r2}	ω_{t1}	ω_{t2}
PW91-GGA	1588	567	370	280	205	119
RPBE-GGA	1582	572	373	293	178	91

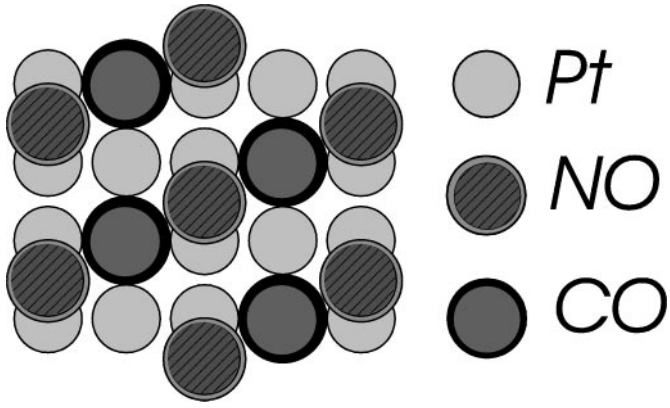

FIG. 3. Sketch of the NO/CO co-adsorption structure within a $c(2\times4)$ cell for $\Theta_{NO} = \Theta_{CO} = 0.5$ ML.

variations in the frequencies, except for the low energy, frustrated translations.

4.3. Co-Adsorption Effects

Also, for the co-adsorption phase of NO and CO, island formation has been observed experimentally (14). The most favorable configuration in a $c(2\times4)$ structure at a total coverage $\Theta_{NO} + \Theta_{CO} = \frac{1}{2}$ ML is formed by rows of alternating NO and CO molecules (see Fig. 3). The adsorption energy (obtained with the PW91-GGA) $E_{ads}^{PW91} = 3.86$ eV is higher than the sum of the single adsorption energies of NO and CO at half coverage ($E_{ads}^{NO} + E_{ads}^{CO} = 3.79$ eV), indicating that the formation of a mixed NO/CO island is favored compared to the formation of two separate islands. Unfortunately, the RPBE functional leads in this case to a qualitative difference: the adsorption energy for the co-adsorption phase is decreased to $E_{ads}^{RPBE} = 3.04$ eV, which is 60 meV less than the sum of the individual adsorption energy of CO ($E_{ads}^{RPBE} = 1.45$ eV) and NO ($E_{ads}^{RPBE} = 1.65$ eV) at half coverage. So although the energy differences between the co-adsorption phase and separately adsorbed species is small for both functionals, they lead to a qualitatively different description of the adsorption process.

Another related co-adsorption effect is the shift in the frequencies upon adsorption: for both species the frequency shifts down w.r.t. the isolated species at $\Theta = 0.25$; $\Delta\omega = 10\ cm^{-1}$ for CO and $30\ cm^{-1}$ for NO. The same effect was observed experimentally (14) ($\Delta\omega_{CO} = 14\ cm^{-1}$; $\Delta\omega_{NO} = 24\ cm^{-1}$). The frequency shift determined within the RPBE-GGA ($\Delta\omega = 26\ cm^{-1}$ for CO and $38\ cm^{-1}$ for NO) are even slightly larger than the PW91-GGA result. The higher frequencies for the separate (CO or NO) islands stem mainly from dipole–dipole coupling of adsorbates of the same type (i.e., same stretching frequency). Since in the co-adsorption phase the CO–CO and NO–NO distances are larger than within the separate islands these frequencies are lower, independent of the adsorption energies.

Summarizing we find that the formation of mixed NO/CO-islands at the surface is—within the error bars of our calculation—thermoneutral, with a lower adsorbate stretch frequency than for the isolated species.

4.4. Adsorption of Atoms

Modeling of the reaction pathways and calculating the relevant reaction barriers requires the knowledge of reasonable starting, intermediate, and final configurations. Until now only the starting configuration with the NO/CO co-adsorption phase was discussed. For all other situations we are mainly concerned with free molecules and adsorbed atoms which we will discuss here. The species of interest are oxygen and nitrogen atoms.

4.4.1. Oxygen Adsorption

According to our calculations, oxygen adsorbs at every coverage preferentially in bridge positions, in agreement with the findings of an earlier DFT study (36). Adsorbing oxygen at the Pt(100) surface at a coverage of $\Theta_O = \frac{1}{4}$ ML in a $c(2\times4)$ arrangement leads to an adsorption energy of $E_{ads}^{PW91} = 2.10$ eV/molecule ($E_{ads}^{RPBE} = 1.44$ eV); adsorption in hollow sites would result in 0.72 eV/molecule less. The height above the surface is 1.36 (1.03 Å) for the bridge (hollow) site. Decreasing the oxygen coverage to $\Theta_O = \frac{1}{6}$ ML in a $p(2\times3)$ arrangement increases the adsorption energy by 180 meV (PW91-GGA) at an essentially unchanged adsorption geometry.

4.4.2. Nitrogen Adsorption

In the case of nitrogen the situation is completely different. Nitrogen adsorption on Pt(100) is an endothermic process (37). Furthermore the potential energy surface describing N adsorption on the surface is very flat, so that the adsorption energies for bridge and hollow adsorption are rather similar and the site preference depends on the coverage (cf. Table 4). These rather small differences in adsorption energies favor surface diffusion of nitrogen and hence the desorption of N_2, where first two N atoms have to find each other before they can recombine. This high mobility of nitrogen is an additional requirement for the explosive occurrence of N_2 desorption. Similar trends are

TABLE 4

Adsorption Energies (per N_2 Molecule) and Heights above the Surface for Nitrogen Adsorption on Pt(100) in Bridge and Hollow Positions at Various Coverages

	1/3		1/6	
Θ site	*b*	*h*	*b*	*h*
E_{ads}^{PW91} (eV)	−1.72	−1.86	−1.72	−1.67
h (Å)	1.23	0.85	1.24	0.81

obtained for the RPBE-functional, with an adsorption energy of 1.68 eV at the bridge position $\Theta = \frac{1}{6}$ ML). However, co-adsorbed with O, both species favor bridged positions at reduced adsorption energies due to repulsive interaction.

5. REACTION BARRIERS

The major part for the energy profile describing the CO/NO reaction over the Pt(100) surface can now already be constructed. Missing are only the reaction barriers for NO dissociation, N_2 desorption, and finally CO oxidation.

5.1. NO Dissociation

The first and most important reaction step, which is considered to be rate limiting for the NO/CO redox reaction, is the dissociation of NO at the surface. We forget for the moment about the co-adsorbed carbon-monoxide at the surface and consider only the dissociation of NO on a clean Pt(100) surface. The analysis of this dissociation process is done by employing the nudged elastic band method described in Section 3. The starting configuration is a bridge-adsorbed NO molecule and the reaction ends up with nitrogen and oxygen co-adsorbed at the surface. Taking into account that the nitrogen may occupy bridge as well as hollow sites at the surface, we investigated several different pathways, the best of which is shown in Fig. 4. From the calculation of the frequencies of adsorbed NO, we expect already the lowest frequency, namely the frustrated translation to initiate the reaction, which is confirmed by the calculation. The NO molecule simply tilts down, dropping the oxygen atom at the neighboring bridge site,

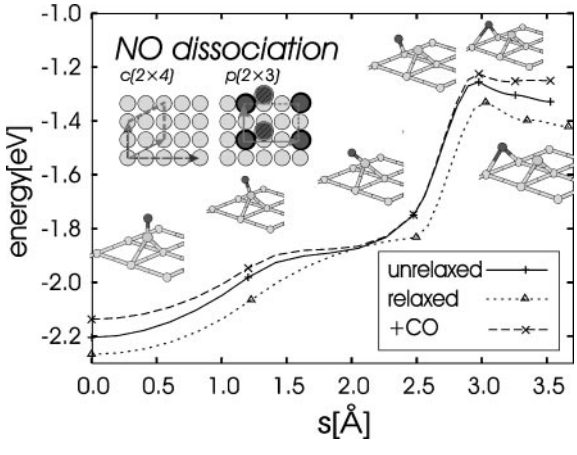

FIG. 4. Dissociation of NO over Pt(100) at $\Theta_{NO} = \frac{1}{2}$-ML cell. Shown is the optimum reaction path from the nudged-elastic-band calculation (solid line) and the potential energy along this pathway (energy zero equals a free NO molecule). The dotted (dashed) line illustrates the effect of including substrate relaxation (co-adsorbing CO). Calculations for the unrelaxed/relaxed data have been preformed within the $c(2 \times 4)$ cell, for the co-adsorbed CO in a $p(2 \times 3)$ with the geometry for the initial state as indicated in the inset (carbon black, oxygen of NO dashed).

while the nitrogen remains essentially at the same bridge site. We determine an energy barrier of $E_{act}^{PW91} = 0.96$ eV ($E_{act}^{RPBE} = 1.26$ eV) located at the very end of the reaction path (i.e., close to the final state). At this point the molecule is already extended to $d = 2.01$ Å, with the molecules already at the heights of the atomic adsorption (see Fig. 5a). The minimum formed by the N/O co-adsorption phase is only a very shallow one. Experimentally a NO dissociation barrier of 1.24 eV was estimated (19). Decreasing the coverage to $\Theta_{NO} = \frac{1}{6}$ (i.e., enlarging the super cell to $p(2 \times 3)$) influences neither the barrier nor the dissociation pathway. All other transition states connected to different reaction scenarios are much higher in energy, so that only the depicted state will be of significance. Comparing this reaction scenario with the co-adsorption phase from Fig. 3, it becomes immediately obvious that the dissociation is inhibited at this high coverage. The CO flanking the NO molecules block both bridge sites, so that the reaction path is effectively inhibited. As soon as somewhere at the surface (possibly at steps or defects) a CO or NO molecule desorbs, the first NO molecule may dissociate and induce the chain reaction leading finally to NO reduction and the oxidation of CO. In order to check for any electronic influence of co-adsorbed CO we recalculated the barrier in the larger $p(2 \times 3)$ cell and placed also one CO molecule at a neighboring on-top site (see inset in Fig. 4). The result is shown in Fig. 4 (dashed line). CO increases the potential energy of the NO and the dissociation products N/O slightly. But at the same time also the energy at the transition state itself is increased, so that the net effect is only $\Delta E_{act}^{CO} = -50$ meV. Similarly we investigated the influence of substrate relaxation on the barrier height, by starting from the relaxed pathway and included the upper Pt layer in the optimization process of the reaction pathway. The dotted curve in Fig. 4 shows the result. Similar to the co-adsorption effect the whole transition path shifted in the same direction, this time to lower energies, so that the net effect remains again small ($\Delta E_{act}^{relax} = -20$ meV). These results justify the assumptions of neglecting substrate relaxation.

5.2. N_2 Desorption

The step following immediately after the dissociation of NO is the recombinative desorption of N_2 from the surface. Therefore two dissociated NO molecules are necessary, so that the molecule can be formed.

In Fig. 6 our results for the N_2 desorption within a $p(2 \times 3)$ cell are shown: combined with a very low energy barrier of about $E_{act}^{PW91} = 90$ meV (see Fig. 5) both N atoms approach each other and start forming an N_2 molecule. Using the RPBE functional the process is even nonactivated. So for both functionals the reaction will be governed mainly by the diffusion barrier $E_{diff}^{RPBE} \sim E_{diff}^{PW91} \sim 100$ meV.

Along the reaction pathway we identified two other local minima—a $\pi - \sigma$ bound configuration over bridge and

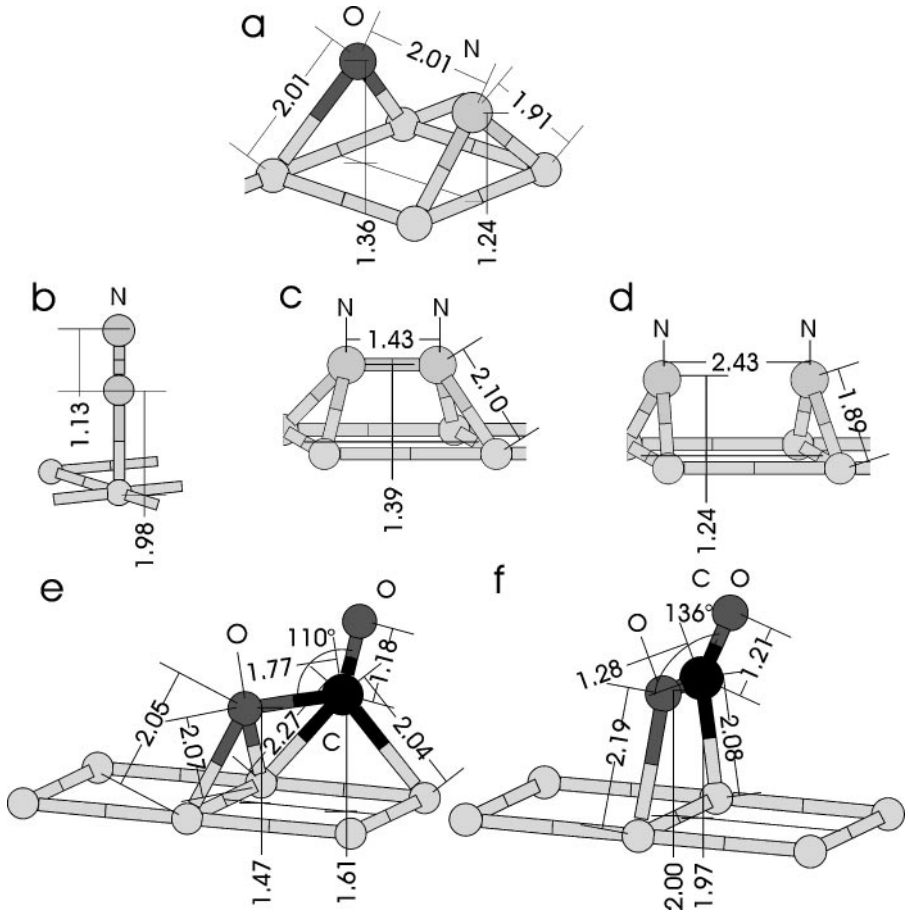

FIG. 5. Optimized geometries for the transition states of NO dissociation (a), N_2 desorption (d), CO oxidation (e), and the molecularly adsorbed configurations of N_2 (b, c) and CO_2 (f).

an on-top adsorbed upright one with adsorption energies within the PW91-GGA (RPBE-GGA) of 0.1 eV (−0.62 eV) and 0.25 eV (−0.53 eV), respectively. These geometries are also sketched in Fig. 5. Two very similar molecular states were very recently identified for N_2 desorption from Pt(111) (38). However, this does not exclude other (more stable) molecular adsorption geometries at steps or kinks at the surface, as it has been shown by Tripa and co-workers (39).

Our findings of a negligible (or even vanishing) energy barrier in combination with the high mobility of nitrogen on the surface implies the immediate formation of N_2 and desorption after NO dissociation, as it was observed experimentally (15).

5.3. CO Oxidation

Finally we come to the last reaction step: the CO oxidation. Again the lowest energy pathway together with sketches of the intermediate configurations is shown in Fig. 7 (for PW91-GGA). First the CO molecule approaches the oxygen via a bridge site, where we find a small shoulder along our reaction path. Reducing the oxygen–CO distance further leads still to an energy increase, until the transition state at an energy barrier of $E_{\mathrm{act}}^{\mathrm{PW91}} = 0.82$ eV ($E_{\mathrm{act}}^{\mathrm{RPBE}} = 0.87$ eV). From here the potential energy decreases continuously, leading to a weakly bound CO_2 molecule, which finally desorbs from the surface. The geometries for the transition state and the bonded CO_2 molecule are sketched in Figs. 5e and 5f. Since we were using a vertical desorbing CO_2 molecule for the final configuration, the molecule has to turn upright before desorbing. In the case of a realistic desorption, we expect from the geometry of the physisorbed CO_2 molecule a nearly horizontal desorption geometry. This reaction path is very similar to that determined in our previous study for the CO oxidation over the Pt(111) surface (33, 40). However, the calculated barrier is slightly higher on Pt(100) than on Pt(111) ($E_{\mathrm{act}}^{(111)} = 0.75$ eV with PW91-GGA (33). This is the consequence of larger distances between the reacting atoms on the more open (100) surface. While larger distances favor the initial configuration, leading to higher adsorption energies, the energy at the TS becomes less favorable, since the new formed bonds have to be longer and hence less strong. Both effects sum up to a higher activation energy.

Finally we checked again the influence of substrate relaxation on the geometry and energetics of the reaction

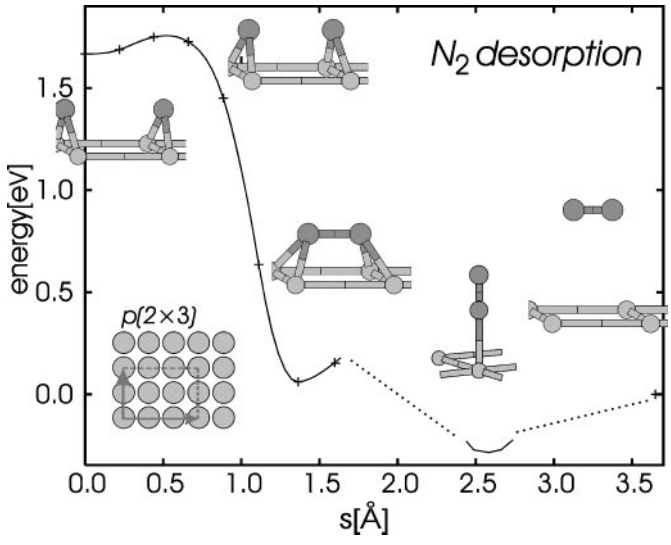

FIG. 6. Recombinative desorption of N_2 over Pt(100) at $\Theta_N = \frac{1}{3}$ ML in a $p(2 \times 3)$ cell. Shown is the optimum reaction path from the nudged-elastic-band calculation and the potential energy (PW91-GGA) along this pathway (energy zero equals a free N_2 molecule). The connection between the two local molecular minima and for the desorption of the first molecular state are only sketched (dashed lines) and not calculated.

pathway (dashed line in Fig. 7). Also in this case we find a comparable decrease in energy for the starting configuration and the transition state, so that the barrier height remains nearly unaffected ($\Delta E_{\text{act}}^{\text{relax}} = -30$ meV). Relaxing the substrate also adds a shallow local minimum immediately after the transition state to the path.

It should not remain unmentioned that the same transition state is relevant for the CO–O_2 reaction, which exhibits a similar oscillating behavior and was subjected to many studies (7).

5.4. Direct NO/CO Redox Reaction

Based on these findings there is still a pathway imaginable that has been neglected so far: a direct reaction of NO and CO, where the CO molecule reacts directly with a nascent oxygen atom from the NO dissociation. To check for that we had to choose a high coverage, so that the CO molecule is close enough to catch the oxygen atom from the dissociation process. The optimized pathway is shown in Fig. 8. The reaction barrier is much higher (E_{act} =2.28 eV) than the barriers we found for the single reaction steps. A more detailed investigation of this reaction scenario gives the reason: The CO molecule blocks partially the Pt-Pt bridge which has to attract the oxygen atom to enable the NO dissociation process. So the carbon monoxide has to attract the oxygen instead of the platinum atom, which on the other hand leads to a strong weakening of the CO-Pt bond. This implies that both barriers (NO dissociation and CO oxidation) have to be overcome simultaneously, before the energy from the N_2 desorption can be gained. This energy gain (as indicated by the lower curve in Fig. 8) can only be realized after the NO molecule is dissociated completely, i.e., after the transition state is crossed. This analysis shows that the model involving several reaction steps is justified and explains also the experimentally observed correlation between the ability of the platinum surface to dissociate NO and the reaction rate of the CO/NO reaction.

6. ENERGY PROFILE

From the results in Sections 4 and 5 we have accumulated enough information to describe the energetics of the entire reaction. Such an energy profile is depicted in Fig. 9,

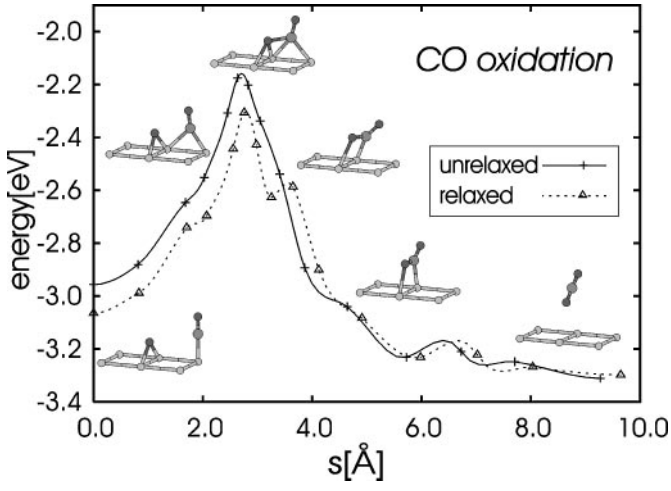

FIG. 7. Oxidation of CO by O over Pt(100) in a $p(2 \times 3)$ cell. Shown is the optimum reaction path from the nudged-elastic-band calculation and the potential energy (PW91-GGA) along this pathway (energy zero equals a free CO plus half an O_2 molecule). The dotted line illustrates the effect of substrate relaxation.

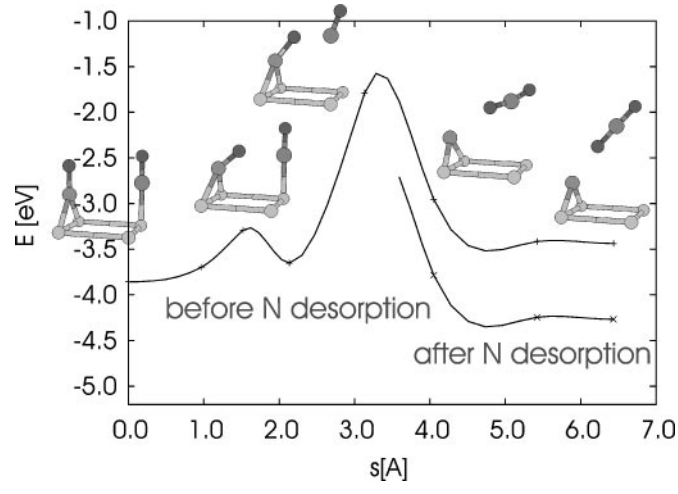

FIG. 8. Direct redox reaction of NO and CO over Pt(100) in a $c(2 \times 4)$ cell. Shown is the optimum reaction path from the nudged-elastic-band calculation and the potential energy (PW91-GGA) along this pathway (energy zero equals to the free NO and CO molecule). The lower curve indicates the energy gain due to N_2 desorption.

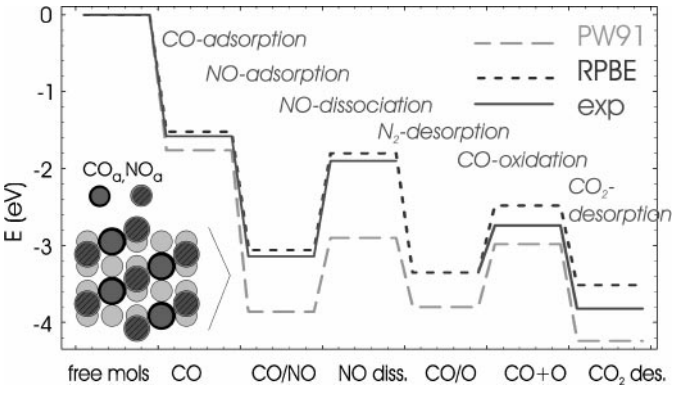

FIG. 9. Energy profile for the NO reduction by CO over Pt(100). The energy zero is set equal to the energy of the gas-phase molecules. The solid line is drawn on the basis of experimental values from (18, 19); the dashed(dotted) line corresponds to calculated values using the PW91-(RPBE-) GGA functional. The inset in the lower left shows the co-adsorption structure for CO and NO at a coverage of 0.5 monolayer.

showing the values obtained with the PW91-GGA and RPBE-GGA together with the post-optimized experimental values from (18, 19). The reaction starts at the left end of the profile, where the energy zero has been set to the energy of NO and CO molecules in the gas phase. Going to the right first CO becomes adsorbed followed by co-adsorbed NO. Then the energy barrier to NO dissociation has to be overcome, which is only possible if a CO molecule desorbs previously ("vacancy requirement"). The following unstable configuration of N/O/CO co-adsorption becomes significantly stabilized by the recombinative desorption of $\frac{1}{2}N_2$. Finally the CO molecule is oxidized and desorbs as CO_2 from the surface.

At this point it is appropriate to return to the influence of the GGA functional. As we have emphasized in the Introduction, both functionals lead to essentially identical adsorption- and transition-state geometries. The lower adsorption energies obtained with the RPBE functional reflect the trend to correct the overbinding characteristic for the LDA and still present in the PW91-GGA functional. Activation energies, however, are found to be slightly increased, especially for the NO dissociation. Here the important point is that in this late transition state we have essentially three adsorbate/substrate bonds (N/O/CO), compared to two in the initial state. The RPBE corrections are therefore stronger at the TS than in the initial state, leading to an increased activation energy. In the case of CO oxidation the number of bonds does not change during the reaction so the activation energies for both GGA functionals are essentially equal.

7. REACTION RATES

What we derived so far is the energetic profile of the lowest energy reaction pathway connecting the reactants NO and CO and the products N_2 and CO_2, as it is shown in Fig. 9. However, the reaction is not determined by the activation energies alone. In its simplest form the kinetics of a single reaction step can be described with an Arrhenius-type expression for the reaction rate constant k

$$k = \nu \cdot e^{-\frac{E^0_{\rm act}}{k_{\rm B}T}} \qquad [3]$$

at a temperature T with the attempt frequency (or preexponential) ν, the zero-point corrected activation energy $E^0_{\rm act}$ and Boltzmann's constant $k_{\rm B}$. The reaction rate r is then related to the rate constant via a function $f(\Theta_i)$ dependent on the coverage Θ of the reactants i:

$$r = k \cdot \prod_i f(\Theta_i). \qquad [4]$$

In a simple model this dependency can be described employing reaction orders x_i as $f(\Theta_i) = \Theta_i^{x_i}$.

In this section we will address the entropic contributions to the reaction under the assumption of the validity of harmonic transition-state theory. From the vibrational spectra at all adsorption and transition-state configurations the preexponentials of the corresponding rate equations can be calculated via the partition functions in the initial ($f_{\rm ini}$) and transition state ($f_{\rm TS}$) (41)

$$\nu = \frac{k_{\rm B}T}{h} z \frac{f_{\rm TS}}{f_{\rm ini}}, \qquad [5]$$

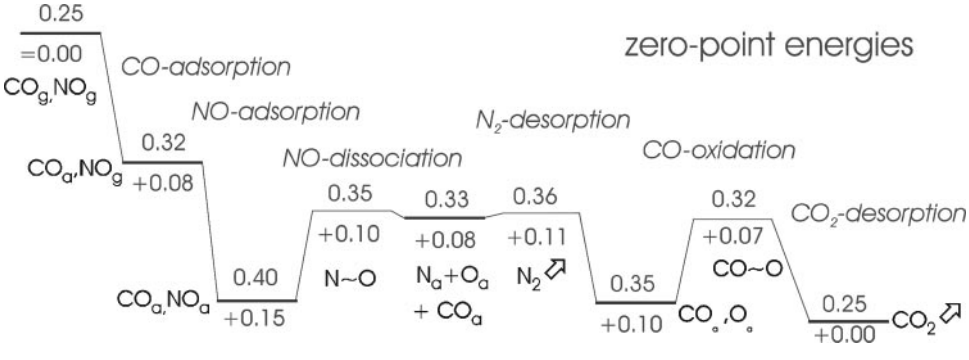

FIG. 10. Relevant zero point energies (in eV) during the reaction. Values below the profile are w.r.t. to the gas-phase molecules NO and CO.

where h is Planck's constant and z is 1 for all reactions, but NO dissociation, where $z = 2$, accounts for the two equivalent dissociation pathways out of the bridge position. The (vibrational) partition function

$$f = \frac{k_B T}{h} \prod_i \left(1 - e^{-\frac{h\nu_i}{k_B T}}\right)^{-1} \quad [6]$$

for the tightly bound initial and transition states is calculated from the normal mode frequencies ν_i, obtained by diagonalizing the dynamical matrix. Force constants are calculated from the Hellmann–Feynman forces acting on the atoms in slightly distorted configurations of the adsorbate complex. For the loosely bound transition states in the desorption reactions the molecular partition function is given by the product of the vibrational partition function of the free molecule and the rotational partition function $f_{rot} = 8\pi^2 I k_B T/h^2$ with the momentum of inertia of the molecule I. The results for the preexponentials are shown in the upper panel of Fig. 11.

The prefactors are all within the usual range of 10^{11}–10^{14} ML $\cdot$ s^{-1} and do not show any peculiarity in their behavior. The second quantity of relevance for the reaction derived from the frequency spectra is the vibrational zero point correction to the activation energy $\sum_i \frac{1}{2} h\nu_i$.

The calculated values are given in Fig. 10. Although the absolute value of the energy correction is generally rather small, it destabilizes the adsorption structures by up to 150 meV (CO/NO co-adsorption structure). The maximum correction to the relative barrier heights are 50 meV for the NO dissociation, equivalent to a factor of 4.2 in the dissociation rate (at 400 K). All prefactors and zero-point energies reported are based on frequency spectra calculated within the PW91-GGA. We have checked the influence of the xc-functional on prefactors and zero-point energies explicitly for NO dissociation. On the basis of the RPBE-frequencies, we obtain a prefactor $3.4 \cdot 10^{13}$ ML $\cdot$ s^{-1}, which is a factor of 1.6 higher than the corresponding PW91-GGA value. Also the zero-point corrections differ by 8 meV, resulting in an additional factor in the rate (at 400 K) of 1.25. So overall, the different sets of frequencies introduce a factor of 2 in the reaction rate, which is equivalent to an error in the activation energy of less than 20 meV. Since we do not expect our energies to be more accurate than this, the assumption of same frequencies for both functionals is justified.

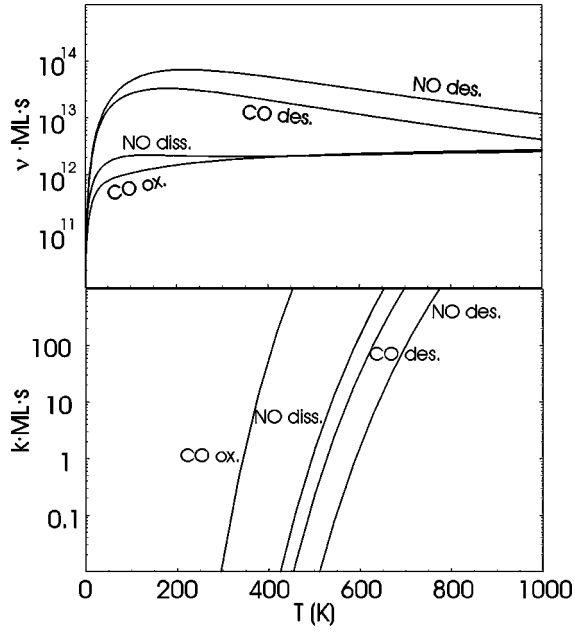

FIG. 11. Preexponentials and reaction rates for the main processes.

Combining the activation energies from the previous section with the prefactors and zero-point corrections calculated here, we can calculate the reaction rates as a function of temperature according to Eq. [3].

The results are plotted in the lower panel of Fig. 11. Values for $T = 400$ K are compiled together with the experimental estimates in Table 5. In the rate constants for the desorption steps, the differences due to the xc-functional are obvious: while the values from PW91-GGA are up to seven orders of magnitude off, the values obtained with RPBE-GGA agree within two orders of magnitude. Since for these reaction steps also the experimental prefactors are at typical values around 10^{14}, the degree of agreement is determined almost by the adsorption energies alone. This shows once more the problems discussed above: from the calculations

TABLE 5

Calculated (Zero-Point Corrected) Activation Energies E^0_{act} (eV), Preexponential Factors and Rate Constants k in (ML $\cdot$ s)$^{-1}$ at $T = 400$ K Compared to Experimental Values from (18, 19)

	PW91-GGA				RPBE-GGA				Exp.		
Process	E_{act}	E^0_{act}	ν	k	E_{act}	E^0_{act}	ν	k	E_{act}	ν	k
CO des.	1.72	1.64	$2.1 \cdot 10^{13}$	$4.1 \cdot 10^{-8}$	1.45	1.37	$2.1 \cdot 10^{13}$	$1.0 \cdot 10^{-4}$	1.50	$1.0 \cdot 10^{14}$	$1.4 \cdot 10^{-5}$
NO des.	2.07	2.00	$5.3 \cdot 10^{13}$	$3.3 \cdot 10^{-12}$	1.65	1.58	$5.3 \cdot 10^{13}$	$6.4 \cdot 10^{-7}$	1.48	$1.7 \cdot 10^{14}$	$4.4 \cdot 10^{-5}$
NO diss.	0.96	0.91	$2.1 \cdot 10^{12}$	$7.5 \cdot 10^{0}$	1.26	1.21	$2.1 \cdot 10^{12}$	$1.2 \cdot 10^{-3}$	1.24	$2.0 \cdot 10^{15}$	$5.2 \cdot 10^{-1}$
N_2 des.	0.09	0.15	$2.1 \cdot 10^{13}$	$3.6 \cdot 10^{11}$	—	—	—	—	—	—	—
CO + O	0.82	0.78	$2.0 \cdot 10^{12}$	$2.6 \cdot 10^{2}$	0.87	0.83	$2.0 \cdot 10^{12}$	$6.1 \cdot 10^{1}$	0.61	$2.0 \cdot 10^{9}$	$4.5 \cdot 10^{1}$

integral adsorption energies are obtained which lie above the isosterical values, describing the de-/adsorption behavior at a given coverage. The RPBE-GGA causes a reduction of the adsorption energy, bringing it close to the isosteric value.

For the reaction steps NO dissociation and CO oxidation the situation is slightly different: Here the prefactors used in the kinetic modeling of (18, 19) differ by three/four orders of magnitude, respectively, from those derived from the vibrational spectra. However, the reaction rates (obtained for both xc-functionals) coincide again with the experimental values within one to two orders of magnitude.

From this two conclusions can be drawn: first, the ambiguity in xc-functionals affects mainly adsorption energies. For activation energies, the influence (and therefore the error due to the approximations in the xc-functional) is much smaller. A similar conclusion was derived for a similar reaction over Pd surfaces (42).

Second, for "true" reaction steps, the inclusion of kinetic effects (i.e., prefactors) is crucial for a comparison with experimentally derived values. A reason for this might be the difficulties in extracting prefactors and activation energies from experimentally observed reaction rates.

8. CONCLUSIONS

Summarizing we have shown:

- NO adsorbs on the surface exclusively in bridge sites and forms a pseudo-hexagonal layer with a $c(2 \times 4)$ structure at $\Theta = \frac{1}{2}$ ML.
- Co-adsorption of CO and NO leads to the formation of mixed islands with a row-wise arrangement structure of alternating NO and CO molecules. Within these islands the frequencies of both adsorbates shift down w.r.t. the separate adsorption of both gases.
- NO dissociation is activated by $E_{\text{barr}}^{\text{PW91}} = 0.96$ eV ($E_{\text{barr}}^{\text{RPBE}} = 1.26$ eV), under the assumption that one of the neighboring CO molecules desorbs.
- N_2 desorption follows immediately after the dissociation of two NO molecules, due to the high mobility of N at the surface and the strong intramolecular bond of N_2; it occurs via molecularly adsorbed intermediates.
- CO oxidation occurs via a pathway very similar to that on Pt(111), but with a slightly lower reaction barrier.
- CO_2 is weakly bound at the surface before desorbing in a flat geometry.
- Using harmonic transition-state theory an accurate determination of reaction rates on the basis of DFT is possible.

ACKNOWLEDGMENTS

Calculations have been performed on the Cray T3E at the John v. Neumann Institute for Computing in the Forschungszentrum Jülich. Financial support by the research center of the Robert Bosch GmbH Stuttgart is gratefully acknowledged.

REFERENCES

1. Somorjai, G., "Introduction to Surface Chemistry and Catalysis" Wiley, New York, 1994.
2. Gorte, R. J., and Schmidt, L. D., *Surf. Sci.* **111**, 260 (1981).
3. Fischer, T. E., and Kelemen, S. R., *J. Catal.* **53**, 24 (1978).
4. Gorte, R. J., Schmidt, L. D., and Gland, J. L., *Surf. Sci.* **109**, 367 (1981).
5. Singh-Boparai, S. P., and King, D. A., "Proceedings, 4th International Congress on Surf. Science, Cannes, 1980," p. 403.
6. Schwartz, S. B., and Schmidt, L. D., *Surf. Sci.* **183**, L269 (1987).
7. Imbihl, R., *Prog. Surf. Sci.* **44**, 185 (1993).
8. van Hove, M. A., Koestner, R. J., Stair, P. C., Bibérian, J. P., Kesmodel, L. L., Bartoš, I., and Somorjai, G. A., *Surf. Sci.* **103**, 189 (1981).
9. Behm, R. J., Hösler, W., Ritter, E., and Binnig, E., *Phys. Rev. Lett.* **56**, 228 (1986).
10. Gardner, P., Tüshaus, M., Martin, R., and Bradshaw, A. M., *Surf. Sci.* **240**, 112 (1990).
11. Norton, P. R., Davies, J. A., Creber, D. K., Sitter, C. W., and Jackman, T .E., *Surf. Sci.* **108**, 205 (1981).
12. Behm, R. J., Thiel, P. A., Norton, P. R., and Ertl, G., *J. Chem. Phys.* **78**, 7437 (1983); *J. Chem. Phys.* **78**, 7448 (1983).
13. Bonzel, H. P., Brodén, G., and Pirug, G., *J.Catal.* **53**, 96 (1978).
14. Banholzer, W. F., and Masel, R. I., *Surf. Sci.* **137**, 339 (1984).
15. Lesley, M. W., and Schmidt, L. D., *Surf. Sci.* **155**, 215 (1985).
16. Fink, Th., Dath, J.-P., Imbihl, R., and Ertl, G., *J. Chem. Phys.* **95**, 2109 (1991).
17. Daté, M., Okuyama, H., Takagi, N., Nishijima, M., and Aruga, T., *Surf. Sci.* **350**, 79 (1996).
18. Hopkinson, A., and King, D. A., *Chem. Phys.* **177**, 433 (1993).
19. Fink, Th., Dath, J.-P., Bassett, M. R., Imbihl, R., and Ertl, G., *Surf. Sci.* **245**, 96 (1991).
20. Meng, B., Weinberg, W. H., and Evans, J. W., *J. Chem. Phys.* **101**, 3234 (1994).
21. Kresse, G., and Furthmüller, J., *Phys. Rev. B* **54**, 11169 (1996); *Comput. Mat. Sci.* **6**, 15 (1996).
22. Vanderbilt, D., *Phys. Rev. B* **41**, 7892 (1990); Kresse, G., and Hafner, J., *J. Phys.: Condens. Matter* **6**, 8245 (1996).
23. Perdew, J. P., and Zunger, A., *Phys. Rev. B* **23**, 5048 (1981).
24. Perdew, J. P., Chevary, J. A., Vosko, S. H., Jackson, K. A., Pederson, M. R., Singh, D. J., and Fiolhais, C., *Phys. Rev. B* **46**, 6671 (1992).
25. Hammer, B., Hansen, L. B., and Nørskov, J. K., *Phys. Rev. B* **59**, 7413 (1999).
26. Henkelman, G., and Jónsson, H., *Phys. Rev. Lett.* **86**, 664 (2001).
27. Eichler, A., and Hafner, J., *Phys. Rev. Lett.* **79**, 4481 (1997).
28. Eichler, A., and Hafner, J., *J. Chem. Phys.* **109**, 5585 (1998).
29. Eichler, A., and Hafner, J., *Phys. Rev. B* **57** 10,110 (1998).
30. Methfessel, M., and Paxton, A., *Phys. Rev. B* **40**, 3616 (1989).
31. Mills, G., Jónsson, H., and Schenter, G. K., *Surf. Sci.* **324**, 305 (1995).
32. Ulitsky, A., and Elber, R., *J. Chem. Phys.* **92**, 1510 (1990).
33. Eichler, A., and Hafner, J., *Phys. Rev. B* **59**, 5960 (1999).
34. Yeo, Y. Y., Vattuone, L., and King, D. A., *J. Chem. Phys.* **104**, 3810 (1996).
35. Feibelman, P. J., Hammer, B., Nørskov, J. K., Wagner, F., Scheffler M., Stumpf, R., Watwe, R., and Dumesic, J., *J. Chem. Phys. B* **105**, 4018 (2001).
36. Ge, Q., Hu, P., King, D. A., Lee, M.-H., White, J. A., and Payne, M. C., *J. Chem. Phys.* **106**, 1210 (1997).
37. Schwaha, K., and Bechtold, E., *Surf. Sci.* **66**, 383 (1977).
38. Zehr, R., French, C., Haynie, B. C., Solodukhin, A., and Harrison, I., *Surf. Sci.* **451**, 76 (2000).
39. Tripa, C. E., Zubkov, T. S., Yates, J. T., Mavrikakis, M., and Nørskov, J. K., *J. Chem. Phys.* **111**, 8651 (1999).
40. Alavi, A., Hu, P., Deutsch, Th., Silvestrelli, P. L., and Hutter, J., *Phys. Rev. Lett.* **80**, 3650 (1998).
41. van Santen, R. A., and Niemantsverdriet, J. W., "Chemical Kinetics and Catalysis." Plenum Press, New York and London, 1995.
42. Hammer, B., *J. Catal.* **199**, 171 (2001), doi: 10.1006/jcat. 2000. 3147.